Effect of Exposed Facets and Oxidation State of CeO$_2$ Nanoparticles on CO$_2$ Adsorption and Desorption

Gimyeong Seong,* Akira Yoko, Takaaki Tomai, Takashi Naka, Haodong Wang, Anatoly I. Frenkel, and Tadafumi Adschiri*
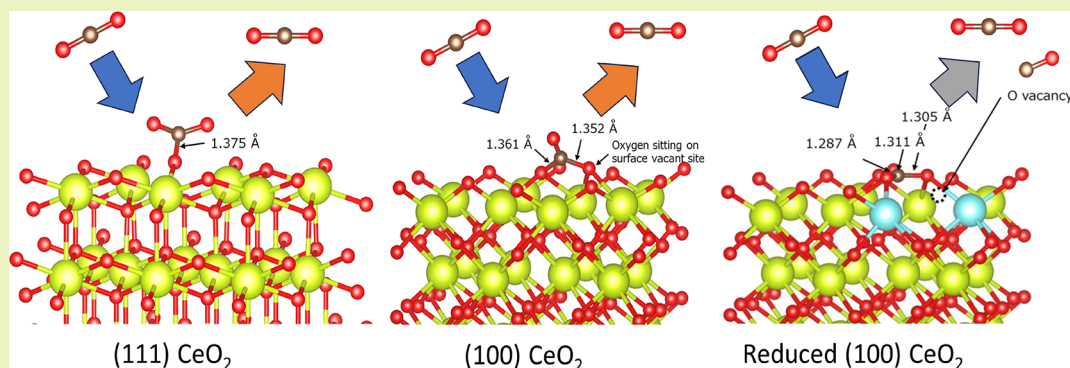
Cite This: https://doi.org/10.1021/acssuschemeng.4c01322

Read Online

ACCESS | Metrics & More | Article Recommendations | Supporting Information

(111) CeO$_2$ (100) CeO$_2$ Reduced (100) CeO$_2$

ABSTRACT: CeO$_2$ nanoparticles exhibit potential as solid adsorbents for carbon dioxide (CO$_2$) capture and storage (CCS), offering precise control over various facets and enhancing their efficiency. This study investigated the adsorption and desorption behaviors of two types of CeO$_2$ nanoparticles: cubic CeO$_2$ with primarily {001} facets and polyhedral CeO$_2$ with mainly {111} facets. The results showed that despite polyhedral CeO$_2$'s lower quantity, it demonstrated successful adsorption−desorption cycles in both oxidized and reduced states. However, reduced CeO$_{2-x}$ exhibited a higher adsorption capacity but displayed irreversible adsorption−desorption cycles. Reversible adsorption occurred through weak bond formation with CO$_2$, while cubic CeO$_2$ with a high oxygen vacancy concentration exhibited irreversible adsorption due to strong bond formation. These insights contribute significantly to understanding CeO$_2$ nanoparticle characteristics and their impact on the CO$_2$ adsorption and desorption processes, aiding in the development of advanced CCS techniques.

KEYWORDS: adsorbent, CeO$_2$, CCS, facet control, oxidation state

INTRODUCTION

Over the past 20 years, there has been an increasing focus on reducing greenhouse gases, such as CO$_2$, to mitigate global warming and air pollution.[1−3] Significant research and development efforts have been made to selectively capture and store CO$_2$.[4−6] Liquid sorbents such as amine and Selexol are commonly used in most industrial carbon dioxide capture and storage (CCS) processes, as evidenced by Yamada's research, which states that they account for 89% of existing large-scale CCS processes.[7] Amino acid salts have recently gained attention as a promising class of adsorbents due to their lower evaporation and degradation rates.[8] This makes them a potentially attractive option for the use in CO$_2$ capture applications. However, due to their high regeneration costs resulting from their decomposition during temperature cycling, solid sorbents are considered as a superior alternative to those liquid sorbents.[9]

In addition, metal−organic frameworks (MOFs), porous carbons, and zeolites have all been studied as potential adsorbents due to their high specific surface area and porosity.[10] MOFs have a low heat capacity, which is advantageous for regeneration since it reduces the energy required.[11] However, MOFs have been found to exhibit weak interactions with CO$_2$ in low-pressure processes, leading to poor performance. Moreover, their sensitivity to the temperature and humidity can result in poor stability.

Metal oxides (e.g., Cs, Mg, and Si), which enable efficient CO$_2$ reversible capture, have been examined as alternative solid adsorbents.[12−16] Especially, CeO$_2$ has a strong interaction with CO$_2$, and numerous mechanistic studies on CeO$_2$ over relatively low temperatures have been conducted.[17−26]

Baumann et al.[27] conducted density functional theory (DFT) calculations, which predicted that the presence of oxygen vacancies makes the adsorption energy of CO_2 more favorable. Additionally, Kumari et al.[28] reported that high concentraion of oxygen vacancies promote the dissociation of CO_2. Recently, Slostowski et al.[29] conducted thermogravimetric analysis to evaluate the adsorption capacity and suitability of CeO_2 nanoparticles as a CO_2 adsorbent.

Recent studies have shown that the surface properties of CeO_2 have a greater impact on the catalytic performance than its specific surface area. For example, in a study by Zhou et al., CeO_2 nanoparticles with similar electrochemical specific areas but different morphologies in partnership with Pt or Pd showed varying performance in methanol and formic acid fuel cells.[30] Therefore, CeO_2, with specific exposed crystal facets and a large specific surface area, holds great potential as a solid adsorbent for CO_2. Specifically, cubic CeO_2 with relatively unstable {001} facets exposed can form oxygen vacancies through activation of oxygen at medium-low temperatures, which is advantageous for CO_2 adsorption.[31,32]

The synthesis of cubic CeO_2, also known as CeO_2 nanocubes with {001} facets, can be achieved by using an environmentally friendly and sustainable method known as supercritical hydrothermal synthesis. This method utilizes water as a solvent and is highly advantageous for producing nanoparticles due to its reactivity and excellent solvent power.[33−40] Recent research has demonstrated the scalability and potential for mass production of CeO_2 nanocubes through a continuous flow synthesizer, making them highly valuable for industrial applications.[37,38] The authors' research group has confirmed high catalytic activity for the reforming of carbonaceous materials, such as heavy oil, lignin, and methane, at low temperatures (300−400 °C) using CeO_2 nanocubes with high oxygen vacancies. This suggests the tunable interaction of carbon atoms with CeO_2[33−37] under oxidation or reduction conditions.

The above information suggests that CO_2 adsorption is affected by the morphology (exposed surface) of CeO_2 nanoparticles as well as the oxidation state. This information is critical for designing the CO_2 adsorption/desorption process and/or determining operational conditions. Therefore, in this study, the effects of (1) the exposed surface and (2) the oxidation state of CeO_2 on CO_2 adsorption were analyzed. Two facet-controlled CeO_2 systems, cubic CeO_2 with {001} facets vs polyhedral CeO_2 with {111} facets, were employed to elucidate the mechanism of CO_2 adsorption on CeO_2 and demonstrate different morphologies that require different treatment (oxidation/reduction).

■ EXPERIMENTS

Materials. Cubic CeO_2 exposing {001} crystal facets were synthesized through supercritical hydrothermal synthesis with in situ modification originally developed by this research group. For characterization and CO_2 adsorption−desorption, the organic modifier was removed via post-treatment (calcination). The synthesis and post-treatment methods were the same as previously reported methods.[33,37] Polyhedral CeO_2 exposing multifacets (mainly {111} facets) was purchased from Sendai Wako Pure Chemicals Ltd. (544841, CeO_2 nanopowder, < 25 nm Sigma-Aldrich, Japan) and used without further treatment. Various high-purity gases (G1 grade, CO_2, Ar, O_2, He, 4% O_2 in Ar, and 4% H_2 in Ar) were purchased from Tanuma Sanso Shokai Co., Ltd. and used without further purification. Pure hydrogen gas was obtained using a hydrogen generator via water

electrolysis (Precision Hydrogen 300; Peak Scientific Instruments, UK).

Characterization. For morphological analysis, high-resolution transmission electron microscopy (HR-TEM, Topcon, Japan, EM-002B, 200 kV, LaB6) was used, and local crystal diffraction patterns were obtained using selected-area electron diffraction (SAED). The SAED patterns were analyzed using *SingleCrystal* (CrystalMaker Software Limited, UK, version 4.1.4). The crystallographic phases of the powder CeO_2 nanoparticles were analyzed using powder X-ray diffraction (XRD, RIGAKU, Japan, Smart Lab 9MTP/RASCO 3 M with Cu Kα radiation, $\lambda = 0.154$ nm, $20 \leq 2\theta \leq 100°$, operated at 45 kV and 200 mA, parallel beam, step = 0.02°). Standard Si (RSRP43275 G, RIGAKU, Japan, $a = 5.4301$ Å) was used for calibration before the sample measurement. No internal standard was used for any of the measurements. Rietveld refinement was performed for all the XRD results using PDXL (RIGAKU, Integrated X-ray powder diffraction software, ver. 2.4.2.0). Raman spectroscopy (HORIBA, Japan, LabRAM HR-800, 532 nm laser excitation used) was used to analyze the internal and surface binding states of CeO_2. The temperature-programmed reduction using hydrogen, H_2-TPR (10% H_2 in He, 50 cm^3/min, 10 °C/min, BELCAT-II, MicrotracBEL Corp. Japan), was used to obtain the oxygen storage capacity (OSC) of CeO_2 after 20% O_2 pretreatment at 400 °C for 30 min.

DRIFTS spectra were collected using a Thermo-Nicolet iS50 FTIR spectrometer equipped with a rapid-scanning option, liquid-nitrogen-cooled mercury cadmium telluride (MCT) detector, and a Praying Mantis high-temperature reaction chamber (Harrick Scientific Products). The experiments were performed at the Structure and Dynamics of Applied Nanomaterials (SDAN) laboratory at the Chemistry Division of Brookhaven National Laboratory. Prior to measurement, each sample was heated at 150 °C for 30 min under He with a flow rate of 20 mL/min to remove surface adsorbed species followed by collection of background spectra under He at room temperature and 400 °C. For the treatment at each temperature, 10% CO_2 (balanced with He, the flow rate is 20 mL/min) was flowed through the reaction chamber for 30 min to acquire CO adsorption spectra followed by flowing He with a flow rate of 20 mL/min for 30 min to acquire CO desorption spectra.

CO_2 Adsorption/Desorption. CO_2 adsorption/desorption was performed by using thermogravimetry differential thermal analysis (TG-DTA) with mass spectroscopy (MS). TG-DTA was performed using STA 2500 Regulus (NETZSCH, Japan), and mass spectrometry (MS) was connected to TG-DTA and performed in real time using JMS-Q1500GC (JEOL Ltd., Japan, see Figure S2 in the SI). Approximately 0.1 g of a sample was placed in the TG sample unit, and the gas type, flow rate, and temperature were controlled for each section of process. The gas concentrations were 10% CO_2, 4% O_2, and 4% H_2 in Ar. Part of the flowing gas was moved to the MS unit in real time using a gas transfer unit and analyzed. The pretreatment conditions and other information for the isothermal adsorption/desorption are described in the Results and Discussion section. For CO_2 temperature-programmed desorption, CO_2-TPD and a BEL-MASS connected to a BELCAT-II instrument (Quadrupole MS, MicrotracBEL Corp., Japan) were used. All samples were pretreated with oxygen (20% in Ar) for 30 min at 400 °C. For producing the reduction state of CeO_2, additional hydrogen pretreatment (10% in Ar) for 2 h at 400 °C was conducted. CO_2 adsorption (10% CO_2 in Ar for 3 h at room temperature) was performed before increasing the temperature. Total flow rate was 50 cm^3/min, and the temperature increase rate was 10 °C/min.

Simulation. Plane-wave basis DFT calculations were conducted to understand the effects of CO_2 adsorption on the CeO_2 surface using the VASP code.[41,42] The generalized gradient approximation proposed by Perdew et al.[43] was employed as the exchange correlation energy functional. The DFT+U method introduced by Dudarev et al.[44] was used to treat electron localization, and the parameter $U−J$ was set to 5.0 eV for Ce 4f.[45] The valence configurations of the pseudopotentials were $5s^2 5p^6 4f^1 5d^1 6s^2$ for Ce, $2s^2 2p^4$ for O, and $2s^2 2p^2$ for C. The energy cutoff for the plane-wave basis was set to 500 eV for all calculations. Slab model calculations were carried out

using 108 atoms for CeO_2 (111) and 216 atoms for the (100) facet with a Monkhorst−Pack k-point mesh of $2 \times 2 \times 1$. The total energy differences were converged to less than 0.001 eV in all calculations. The calculated crystallographic structure models were visualized via VESTA code.[46]

■ RESULTS AND DISCUSSION

Effect of Facet and Oxidation State on Surface Characteristics of CeO_2. Figure 1a shows polyhedral CeO_2
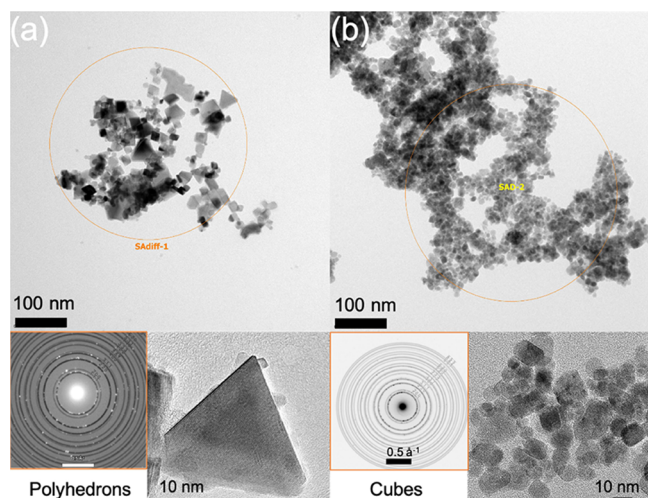

Figure 1. TEM images of different morphology of CeO_2 nanoparticles: (a) nano polyhedrons; (b) nanocubes. Bottom left is the SAED pattern, and bottom right is a high-resolution image, respectively.

nanoparticles. According to the specifications of this sample, the mean particle size was 25 nm, and the particles had a wide size distribution ranging from 5 to 60 nm. In the magnified image of a particle shown in the lower right of (a), well-ordered crystal fringes without defects were observed. The diffraction pattern of the selected area is shown in the lower-left panel of (a). The morphology was diverse and included octahedrons, truncated octahedrons, fragmented octahedrons, and triangles (termed polyhedral CeO_2 in this study). Octahedral CeO_2 mainly exposes the {111} facets, whereas the others have additional {100} and {110} facets. In other words, polyhedral CeO_2 has multiple exposed surfaces (multiple facets).

The exposed facets of CeO_2 can be controlled by adding capping agents that are preferentially adsorbed onto less stable facets (high surface energy). A supercritical hydrothermal synthesis method with in situ capping was used to control the facets of the CeO_2 nanoparticles.[33,37] The cubic nanoparticles prepared in this study have an average size of approximately 10 nm, as shown in Figure 1b. The nanoparticles are well
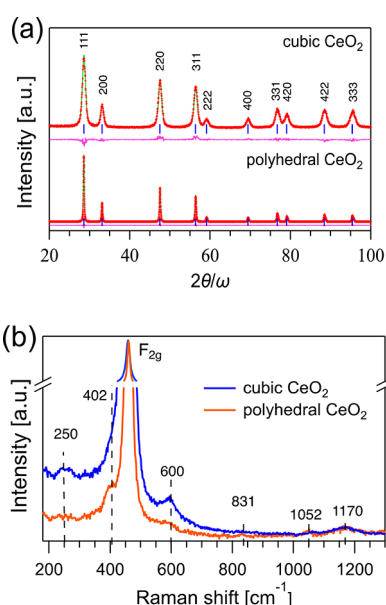
Figure 2. Physical and chemical properties of CeO_2 according to their morphologies: (a) powder XRD peak patterns; (b) Raman spectra (532 nm).
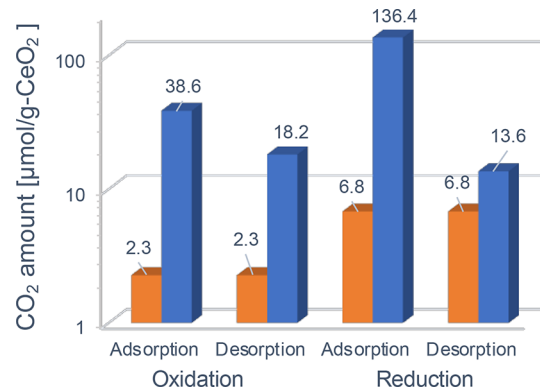
Figure 3. Isothermal adsorption and desorption of CO_2 at 400 °C according to oxidation state of CeO_2: (orange) multifacets exposed polyhedral CeO_2; (blue) {001} facets exposed cubic CeO_2.

dispersed even after calcination. An enlarged high-resolution photograph of the nanoparticles is provided in the bottom-right corner of Figure 1b. Most of the particles show specific crystal faces, mainly judged by the {001} facets, although some particles have rounded corners. The significantly greater OSC values compared to polyhedral CeO_2 support the notion that most particles expose the {001} facets (Table 1). The diffraction pattern of selected particles is shown in (b) (orange circle) on the lower left. This agrees well with the simulated

Table 1. Structural Analysis and Properties of Each CeO_2 Morphology Type
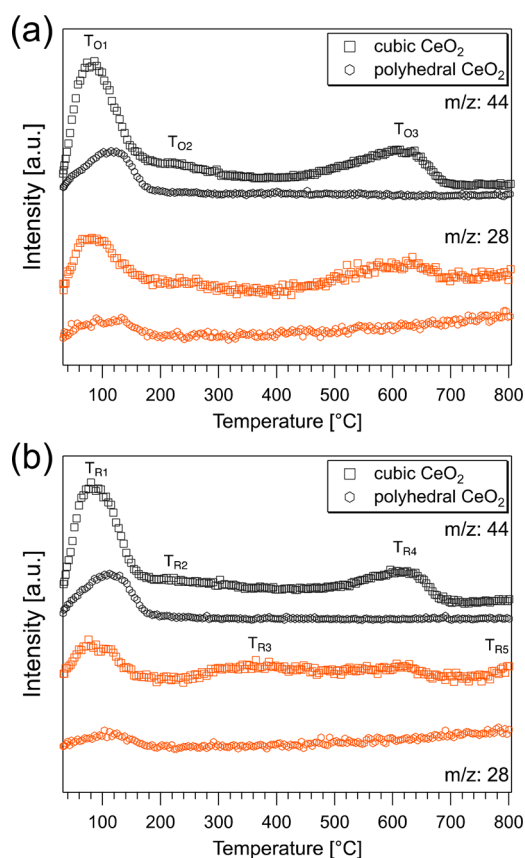
morphology type of CeO_2	crystal size, XRD (TEM) [nm]	lattice constant [nm]	strain [%]	R_{wp} [%]	S	BET [m²/g]	OSC[a] [μmol-O/g] at 400 °C (β)[b]	Ce^{3+} fraction[c] [%]
polyhedrons	28.8 (23.8)	5.4114	0.081	16.24	1.1258	6.57	49 (29)	0.01
cubes	7.2 (8.1)	5.4139	0.26	10.87	1.1432	94.04	198 (123)	0.63

[a]Evaluated using the H_2-TPR method. [b]β region OSC (250−400 °C) in H_2-TPR. [c]Evaluated by magnetic analysis (SI).
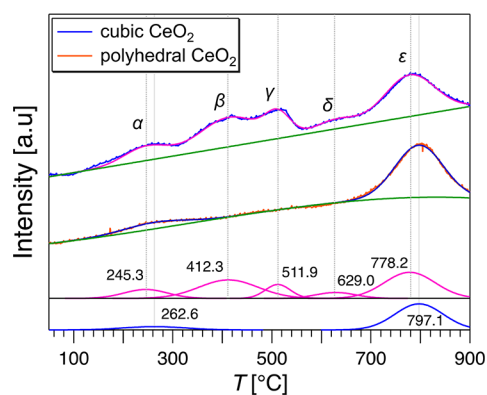
Figure 4. Temperature-dependent reduction behavior of cubic and polyhedral CeO₂ using H₂-TPR. The peaks were fitted using Multipeak Fit of Igor Pro 8 (ver. 8.04).

Figure 5. Temperature-programmed CO₂ desorption (CO₂-TPD) with mass spectrometry (MS) according to oxidation/reduction state and morphology (exposing facet) type of CeO₂ nanoparticles: (a) fully oxidized CeO₂; (b) reduced CeO₂. The m/z 44 represents for CO₂, and m/z 28 represents for CO₂ fragment or CO.

which implied the presence of small nanoparticles. The crystallite size evaluated was 7.2 nm, which is close to that confirmed by the TEM image (mean, 8.1 nm, SD 1.1). These results suggest that both types of CeO_2 particles are single crystals. The specific surface areas of the two CeO_2 samples were significantly different (14.3 times greater for cubic CeO_2 than for polyhedral CeO_2). Compared with polyhedral CeO_2, another characteristic of cubic CeO_2 observed in the XRD results is the lattice distortion and expansion of the lattice constant. This is attributed to the smaller crystal size and the formation of oxygen defects.[31,32,38,49−52]

The surface nature of CeO_2 was analyzed by using Raman spectroscopy (Figure 2b), which revealed the Ce−O bonding state. For both CeO_2 nanoparticles, the peak (402 cm^{-1}) corresponding to the transverse Ce−O stretching vibration was observed. For cubic CeO_2, a red-shift in the F_{2g} mode and broadening occurred (460.2 cm^{-1}) from bulk CeO_2 (465 cm^{-1}), which was probably due to the nanosize effect. Additionally, clear peaks corresponding to the Ce−OH stretching vibration and oxygen vacancy at 250 and 600 cm^{-1}, respectively, were observed in the Raman spectra of cubic CeO_2. In contrast, polyhedral CeO_2 has weaker peaks at 600 and 831 cm^{-1}, suggesting fewer oxygen vacancies and peroxide vibrations (O_2^{2-}).[53] All of these can act as CO_2 adsorption sites.

Effect of Facet and Oxidation State of CeO₂ on CO₂ Adsorption/Desorption. The above results suggest that the CO_2 adsorption/desorption behavior depends on the morphology (exposed facet) of CeO_2 due to the different surface characteristics such as oxygen vacancy that can be affected by the oxidation/reduction treatment of CeO_2.[31−38,54−56] Figure 3 shows the CO_2 adsorption level measured by TG for both polyhedral CeO_2 (orange) and cubic CeO_2 (blue) at 400 °C. Here, a sufficiently high temperature was used to expect complete CO_2 desorption. The CO_2 adsorption/desorption amount was evaluated based on the weight change of CeO_2. The original TG data obtained using MS can be found in the SI (Figures S1 and S2, in the form of wt %). For polyhedral CeO_2, in both the oxidation and reduction states, the adsorption and desorption amounts were the same, indicating reversible CO_2 adsorption. The adsorbed amount was 3-fold higher after reduction treatment. This is likely due to the formation of oxygen vacancies on the CeO_2 particles, which could capture more CO_2 molecules. Thus, this finding led to an improvement in the CO_2 capture process using CeO_2 as an adsorbent by reducing the treatment beforehand.

Compared with polyhedral CeO_2, cubic CeO_2 has a greater amount of CO_2 adsorbed in both the oxidized and reduced states. Similarly to polyhedral CeO_2, the reduced cubic $CeO_{2−x}$ exhibited a 3.53-fold increase in the adsorption capacity compared to its oxidized counterpart. The amount of CO_2 adsorbed on cubic CeO_2 was greater than that desorbed for both the oxidation and the reduction states. In other words, CO_2 desorption is relatively difficult because of the strong interactions between cubic CeO_2 and CO_2. Cubic CeO_2 strongly absorbs CO_2 owing to low CO_2 adsorption energy around oxygen vacancies.[57] Notably, the adsorption of CO_2 on CeO_2 through oxygen vacancies is not solely determined by oxygen vacancy concentration. In our previous study, it was found that small cubic CeO_2 of a few nanometers is easily reduced to the particle core as well as to the surface.[31,32] This means that oxygen is easily released from the surface and can

pattern of CeO_2 (SingleCrystal), which suggests good crystallinity without impurities.
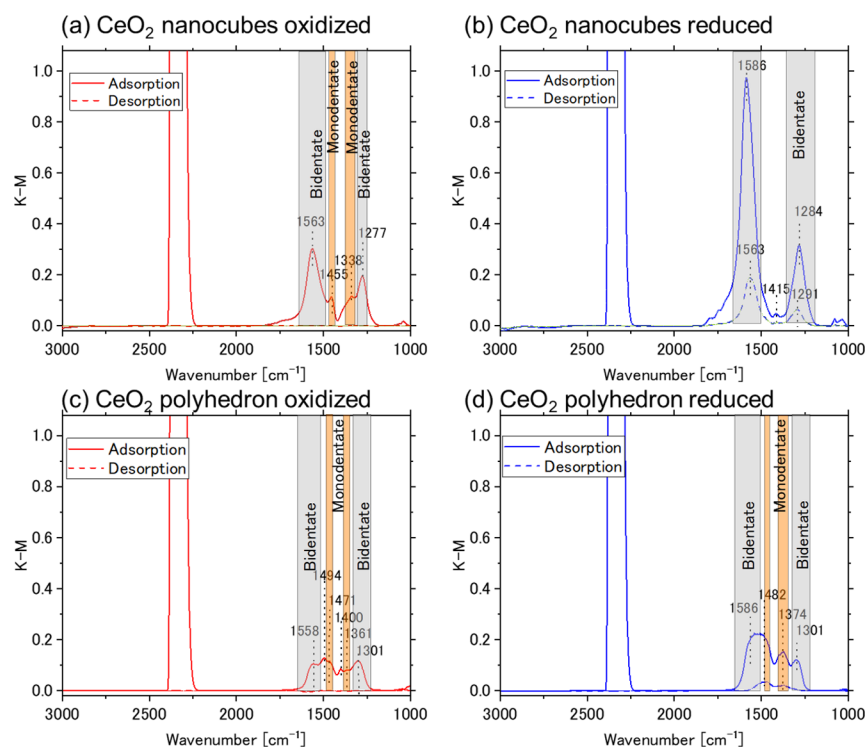
Figure 2a shows the powder XRD peak patterns of the two different types of CeO_2, and the results of the Rietveld refinement are summarized in Table 1. Both samples exhibit a pure CeO_2 peak pattern. The crystallite size of the polyhedral sample, evaluated using the Halder−Wagner method,[47,48] was 28.8 nm, which is similar to the average particle size of 25 nm specified for this sample (TEM, mean 23.8 nm, SD 10.6). For cubic CeO_2, the XRD patterns showed a relatively broad peak,

Figure 6. In situ DRIFTS data at 400 °C with CO_2 adsorption and following desorption with He flow. (a) Oxidized cubic CeO_2 (mainly bidentate-II); (b) reduced cubic CeO_2 (mostly bidentate-II); (c) oxidized polyhedron CeO_2 (monodentate and bidentate-II); (d) reduced polyhedron CeO_2 (monodentate and bidentate-II). Bidentate-II: 1575 and 1294 cm^{-1}, monodentate: 1442 and 1373 cm^{-1}.[65]

diffuse through the particles. This property can provide favorable conditions for the formation of strong carbonate.[19] The stable polydentate configuration requires temperatures of 500 °C or higher for the release of CO_2 to be released. The irreversible CO_2 adsorption observed in cubic CeO_2 at 400 °C, as shown in Figure 3, can be attributed to the strong CO_2 adsorption that mostly occurs in the first step and is irreversible. On the other hand, weaker CO_2 adsorption can be reversible, as confirmed through repeated CO_2 adsorption/desorption cycles (see Figure S3 in the SI).

The above results demonstrate that the number of oxygen vacancies present depends on the exposed facet species and redox treatment, which directly affects the CO_2 adsorption configuration. Freund's group[58] studied the dissociation of hydrogen on the surface of CeO_2 during hydrogen treatment and the change in Ce^{3+} ratio according to annealing temperature. Therefore, it is crucial to examine the CO_2 desorption process based on the number of oxygen vacancies in CeO_2. As shown in Figure 4, the H_2-TPR analysis revealed the reduction tendency of each CeO_2 sample, and the OSC of each CeO_2 sample was evaluated by the amount of hydrogen consumed (see Table 1). For cubic CeO_2, small peaks appeared at around 245 (α) and 629 °C (δ), and relatively large peaks are observed at around 412 (β) and 512 °C (γ). The largest peak was observed at 778.2 °C, (ε). The reducibility of cubic CeO_2 nanomaterials at low temperatures is high compared to other CeO_2-based composite nanomaterials, with a reduction rate of 54.2% up to 540 °C.[31−38] On the other hand, for polyhedral CeO_2, a clear peak was not confirmed in the α, β, γ, δ regions, except the δ region of the high-temperature region. This suggests that cubic CeO_2 is easily reduced even at low temperatures, and the ratio of reduced CeO_{2-x} is high, while polyhedral CeO_2 is not

sufficiently reduced unless the temperature is approximately 800 °C.[59,60]

The relationship between the adsorption strength and oxygen vacancies can be examined. In the case of polyhedral CeO_2, the peak in the β region is very weak, and there is no peak at all around 400 °C. Conversely, for cubic CeO_2, the peak in the β region is larger than that in the α region. This indicates that around 400 °C additional oxygen vacancies were formed, leading to strong CO_2 adsorption. Moreover, the formation of oxygen vacancies typically increases Lewis acidity, resulting in strong adsorption with Lewis bases such as CO_2.[61,62] Although quantifying surface oxygen vacancy points is very difficult, the OSC in the β region is 123 μmol-O/g, which is very close to the irreversible CO_2 adsorption of cubic CeO_2, 122.8 μmol-CO_2/g, suggesting a one-to-one relationship between oxygen vacancy sites and strong carbonate bonding.

Because the reduced state of cubic CeO_2 is accompanied by strong CO_2 adsorption, various desorption patterns are expected depending on the temperature; therefore, the desorption process according to the temperature is examined as follows. Figure 5 shows the temperature-dependent desorption after CO_2 adsorption under an (a) oxygen or (b) hydrogen pretreatment for cubic CeO_2 and polyhedral CeO_2 (CO_2-TPD). For polyhedral CeO_2, CO_2 was desorbed below 180 °C, for both the oxidation state and reduction state. No clear desorption is observed at higher temperatures. Binet et al. reported that 300 °C or higher is required for the desorption of strongly adsorbed CO_2,[19] and Slostowski reported a higher temperature of 500 °C.[29] This result indicated that only weak CO_2 adsorption occurred on the polyhedral CeO_2 surface. On the other hand, for cubic CeO_2, the TPD profiles were more complicated. First, a large amount of CO_2 is desorbed at low temperatures ($T_{O1, R1}$). It is noteworthy that cubic CeO_2 has a
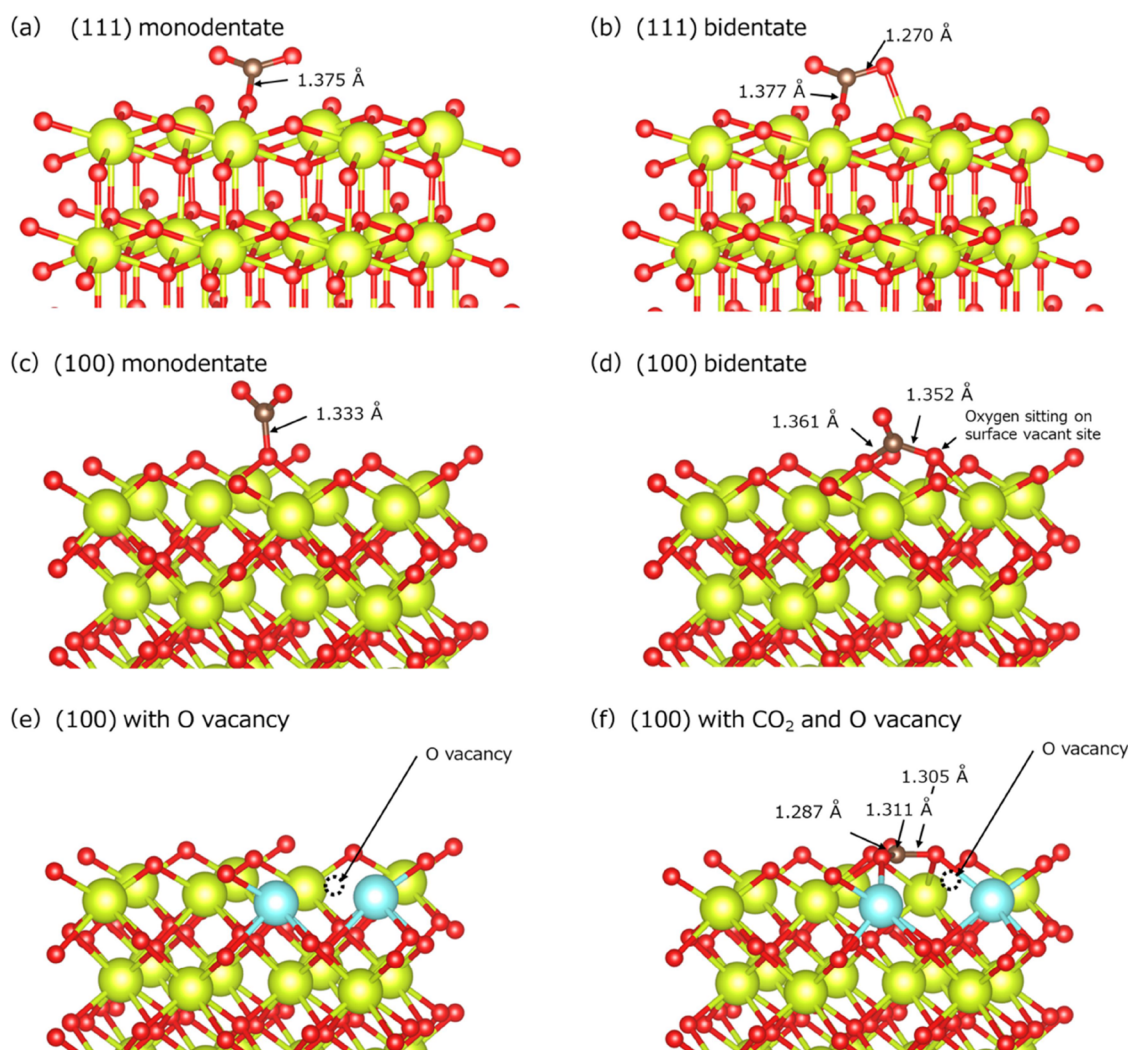
Figure 7. Adsorption state of CO_2 on CeO_2 (111) (a) monodentate, (b) bidentate, and CeO_2 (100) (c) monodentate, (d) bidentate. (e) CeO_2 (100) with an oxygen vacancy, light blue shows Ce^{3+}, (f) strong CO_2 adsorption on CeO_2 (100) with an oxygen vacancy. The simulations were conducted for the slab models, and enlarged figures are shown.

peak position (81.7 °C) lower than that of polyhedral CeO_2 (119.3 °C) in the T_{O1} region. In addition, CO_2 was further desorbed near 200 °C ($T_{O2, R2}$). As demonstrated by the results of isothermal adsorption and desorption, weak CO_2 adsorption occurred even in cubic CeO_2, and it was confirmed that this ratio was also significant. As the temperature rises further, a large peak was detected in the range of temperature from 420 to 670 °C ($T_{O3, R4}$, 620 °C), which corresponds to the strongly bonded CO_2.

The differences between the oxidation and reduction treatments in cubic CeO_2 were clearly observed in the T_{R3} and T_{R5} regions. In the oxidation state, weakly adsorbed CO_2 were almost removed at around 300 °C, whereas a gentle peak continued up to approximately 450 °C for cubic CeO_{2-x}. In the reduced state, continuous desorption occurred from T_{R2} to T_{R4}. In the T_{R3} region, a gentle peak that appeared to be CO, that is, CO_2 dissociative desorption, was observed, rather than the CO_2 fragment peak. The reason for this is that CO_2 adsorption takes place at oxygen vacancy sites of CeO_{2-x}, which can act as reducing sites.[63,64] Typically, this reaction occurs at high temperatures of 800 °C or higher (T_{R5}).[28,33] However, in the case of cubic CeO_{2-x}, it occurred at much

lower temperatures between 250 and 450 °C, likely due to its high reduction potential.

Adsorption and Desorption Mechanism. The adsorption and desorption behaviors of CO_2 on different surface states of CeO_2 were studied using the DRIFTS technique. Figure 6 shows in situ DRIFTS data during the adsorption of CO_2 and the subsequent desorption under an inert atmosphere for both cubic and polyhedron particles with oxidized or reduced states at 400 °C. The adsorption state of CO_2 differed between cubic and polyhedron CeO_2. Specifically, CO_2 tends to be more strongly adsorbed on {001} facets (mainly bidentate-II) compared to {111} facets (mainly monodentate).[65] The reduction of these CeO_2 samples enhances the adsorption of CO_2 because of the formation of oxygen vacancies, which is particularly significant for cubic CeO_2 with a more reducible surface. During the inert gas flow after the introduction of CO_2 introduction, desorption of CO_2 was observed, although remaining adsorbed CO_2 was observed for reduced CeO_2, which is not observed in oxidized CeO_2. These results are consistent with the results of TG measurements for CO_2 adsorption and desorption (Figure 3). The difference in the CO_2 adsorption behavior depending on the morphology and reduction state of CeO_2 originates from the different

bonding states of CO_2. The {001} facets are inherently polar and include surface vacancy sites, whereas the oxidized {111} facets are nonpolar surfaces.

Figure 7 illustrates the adsorption states of CO_2 on CeO_2 (100) and (111) surfaces, which was calculated by first-principles simulations. On (111) surface, the CO_2 adsorption energy was −0.56 eV/molecule for both monodentate and bidentate states (Figure 7a,b). On the contrary, CO_2 adsorption energy for the (100) facet was −1.10 eV/molecule for bidentate state (Figure 7c) while monodentate state did not contribute surface stabilization (+0.26 eV/molecule, Figure 7d). The stoichiometric model of the (100) facet is terminated by an oxygen layer but with half of the vacancy sites because the (100) surface is polar and one of the oxygen atoms of adsorbed CO_2 located on the surface vacant site (Figure 7d), resulting in stronger adsorption. Because of these difference in the surface structure, stronger bidentate adsorption occurs on (100) surface, and the amount of adsorption increases by reducing the surface. Compared to (111) surface, more oxygen vacancies are easily formed on (100) surface and that causes a significant difference in the adsorption energies. When an oxygen vacancy is created on CeO_2 (100) facet, the adsorption energy of CO_2 was found to be −3.40 eV/molecule and the surface stabilization effects was more significant than the stoichiometric surface.

CONCLUSIONS

In this study, the CO_2 adsorption/desorption behaviors of cubic CeO_2 nanoparticles exposed to {001} facets and polyhedral CeO_2 with {111} facets were analyzed under oxidation and reduction conditions. Polyhedral CeO_2 exhibited reversible adsorption in both the oxidized and the reduced states, with a higher adsorption capacity observed in the reduced state. The formation of weaker bonds with adsorbed CO_2 contributed to the reversible adsorption at low temperatures (50−150 °C). In contrast, cubic CeO_2 displayed irreversible adsorption behavior due to the formation of a strong bidentate configuration with oxygen vacancies.

The distinctions in CO_2 adsorption and desorption behaviors, analyzed by TG-DTA with MS, were validated through in situ DRIFTS analysis and DFT calculations, providing insights into molecular behavior. High concentrations of oxygen vacancies induced dissociative desorption of CO_2 even at low temperatures (250−400 °C), significantly lower than that of polyhedral CeO_2 (>800 °C). Consequently, CO_2 adsorption and desorption exhibit dramatic differences depending on the facet species and redox treatment. Therefore, they are expected to contribute to more effective CCS through careful engineering of materials and control of process conditions.

ASSOCIATED CONTENT

Ⓢ Supporting Information

The Supporting Information is available free of charge at https://pubs.acs.org/doi/10.1021/acssuschemeng.4c01322.

CO2 adsorption and desorption TG-DTA original data, MS profiles, cyclic operation result, and Ce^{3+} fraction analysis (PDF)

AUTHOR INFORMATION

Corresponding Authors

Gimyeong Seong − *New Industry Creation Hatchery Center, Tohoku University, Sendai 980-8579, Japan; Department of Environmental and Energy Engineering, The University of Suwon, Hwaseong-si, Gyeonggi-do 18323, Republic of Korea;* ⓘ orcid.org/0000-0003-4292-5936; Phone: +82-31-229-8829; Email: soppua4@suwon.ac.kr; Fax: +82-31-229-8829

Tadafumi Adschiri − *New Industry Creation Hatchery Center, Tohoku University, Sendai 980-8579, Japan; WPI-Advanced Institute for Materials Research (WPI-AIMR), Tohoku University, Sendai 980-8577, Japan;* Phone: +81-22-217-6321; Email: tadafumi.ajiri.b1@tohoku.ac.jp; Fax: +81-22-217-6321

Authors

Akira Yoko − *WPI-Advanced Institute for Materials Research (WPI-AIMR), Tohoku University, Sendai 980-8577, Japan; International Center for Synchrotron Radiation Innovation Smart, Tohoku University, Sendai 980-8579, Japan;* ⓘ orcid.org/0000-0002-1278-272X

Takaaki Tomai − *Institute of Multidisciplinary Research for Advanced Materials, Tohoku University, Sendai 980-8577, Japan;* ⓘ orcid.org/0000-0003-0296-6565

Takashi Naka − *National Institute of Materials Sciences (NIMS), Tsukuba, Ibaraki 305-0047, Japan*

Haodong Wang − *Department of Materials Science and Chemical Engineering, Stony Brook University, Stony Brook, New York 11794, United States*

Anatoly I. Frenkel − *Department of Materials Science and Chemical Engineering, Stony Brook University, Stony Brook, New York 11794, United States; Chemistry Division, Brookhaven National Laboratory, Upton, New York 11973, United States;* ⓘ orcid.org/0000-0002-5451-1207

Complete contact information is available at:
https://pubs.acs.org/10.1021/acssuschemeng.4c01322

Author Contributions

G.S.: conceptualization, methodology, investigation, and writing of the original draft. A.Y.: DFT calculation, review, and editing the manuscript. T.T.: review and editing the manuscript. T.N.: magnetic analysis. H.W. and A.I.F.: DRIFTS analysis. T.A.: conceptualization, supervision, funding acquisition, review, and editing the manuscript.

Notes

The authors declare no competing financial interest.

ACKNOWLEDGMENTS

■ REFERENCES

(1) Skea, J. In Mitigation of climate change summary for policymakers climate change, Working Group III Contribution to the Sixth Assessment Report of the Intergovernmental Panel on Climate Change, 2022. https://www.ipcc.ch/report/ar6/wg3/.

(2) Gambhir, A.; George, M.; McJeon, H.; Arnell, N. W.; Bernie, D.; Mittal, S.; Köberle, A. C.; Lowe, J.; Rogelj, J.; Monteith, S. Near-term transition and longer-term physical climate risks of greenhouse gas emissions pathways. *Nature Climate Change* **2022**, *12* (1), 88−96.

(3) *Global Energy Review 2021*, IEA: Paris, 2021. https://www.iea.org/reports/global-energy-review-2021.

(4) Sgouridis, S.; Carbajales-Dale, M.; Csala, D.; Chiesa, M.; Bardi, U. Comparative net energy analysis of renewable electricity and carbon capture and storage. *Nature Energy* **2019**, *4* (6), 456−465.

(5) Gabrielli, P.; Gazzani, M.; Mazzotti, M. The role of carbon capture and utilization, carbon capture and storage, and biomass to enable a net-zero-CO_2 emissions chemical industry. *Ind. Eng. Chem. Res.* **2020**, *59* (15), 7033−7045.

(6) Noussan, M.; Raimondi, P. P.; Scita, R.; Hafner, M. The role of green and blue hydrogen in the energy transition—A technological and geopolitical perspective. *Sustainability* **2021**, *13* (1), 298.

(7) Yamada, H. Amine-based capture of CO_2 for utilization and storage. *Polym. J.* **2021**, *53* (1), 93−102.

(8) Zhang, Z.; Li, Y.; Zhang, W.; Wang, J.; Soltanian, M. R.; Olabi, A. G. Effectiveness of amino acid salt solutions in capturing CO_2: A review. *Renewable and Sustainable Energy Reviews* **2018**, *98*, 179−188.

(9) Yu, C. H.; Huang, C. H.; Tan, C. S. A review of CO_2 capture by absorption and adsorption. *Aerosol and Air Quality Research* **2012**, *12* (5), 745−769.

(10) Demir, H.; Aksu, G. O.; Gulbalkan, H. C.; Keskin, S. MOF membranes for CO_2 capture: past, present and future. *Carbon Capture Science & Technology* **2022**, *2*, No. 100026.

(11) Lin, Y.; Kong, C.; Zhang, Q.; Chen, L. Metal-organic frameworks for carbon dioxide capture and methane storage. *Adv. Energy Mater.* **2017**, *7* (4), No. 1601296.

(12) Hathaway, P. E.; Davis, M. E. Base catalysis by alkali-modified zeolites: I. Catalytic activity. *J. Catal.* **1989**, *116* (1), 263−278.

(13) Chang Kim, J. C.; Li, H. X.; Chen, C. Y.; Davis, M. E. Base catalysis by intrazeolitic cesium oxides. *Microporous Materials* **1994**, *2* (5), 413−423.

(14) Garcıa-Labiano, F.; Abad, A.; De Diego, L. F.; Gayán, P.; Adánez, J. Calcination of calcium-based sorbents at pressure in a broad range of CO_2 concentrations. *Chem. Eng. Sci.* **2002**, *57* (13), 2381−2393.

(15) Roque-Malherbe, R.; Polanco-Estrella, R.; Marquez-Linares, F. Study of the interaction between silica surfaces and the carbon dioxide molecule. *J. Phys. Chem. C* **2010**, *114* (41), 17773−17787.

(16) Liu, W.; Low, N. W.; Feng, B.; Wang, G.; Diniz da Costa, J. C. Calcium precursors for the production of CaO sorbents for multicycle CO_2 capture. *Environ. Sci. Technol.* **2010**, *44* (2), 841−847.

(17) Binet, C.; Badri, A.; Boutonnet-Kizling, M.; Lavalley, J. C. FTIR study of carbon monoxide adsorption on ceria: $CO_2^{2−}$ carbonite dianion adsorbed species. *Journal of the Chemical Society, Faraday Transactions* **1994**, *90* (7), 1023−1028.

(18) Daturi, M.; Binet, C.; Lavalley, J. C.; Vidal, H.; Kaspar, J.; Graziani, M.; Blanchard, G. Influence of the activation conditions on the elimination of residual impurities on ceria-zirconia mixed oxides. *Journal de Chimie Physique et de Physico-Chimie Biologique* **1998**, *95* (9), 2048−2060.

(19) Binet, C.; Daturi, M.; Lavalley, J.-C. IR study of polycrystalline ceria properties in oxidised and reduced states. *Catal. Today* **1999**, *50* (2), 207−225.

(20) Daturi, M.; Binet, C.; Lavalley, J. C.; Galtayries, A.; Sporken, R. Surface investigation on $Ce_xZr_{1−x}O_2$ compounds. *Phys. Chem. Chem. Phys.* **1999**, *1* (24), 5717−5724.

(21) Daturi, M.; Finocchio, E.; Binet, C.; Lavalley, J. C.; Fally, F.; Perrichon, V. Study of bulk and surface reduction by hydrogen of $Ce_xZr_{1−x}O_2$ mixed oxides followed by FTIR spectroscopy and magnetic balance. *J. Phys. Chem. B* **1999**, *103* (23), 4884−4891.

(22) Daturi, M.; Binet, C.; Lavalley, J. C.; Blanchard, G. Surface FTIR investigations on $Ce_xZr_{1−x}O_2$ system. *Surf. Interface Anal.* **2000**, *30* (1), 273−277.

(23) Daturi, M.; Finocchio, E.; Binet, C.; Lavalley, J. C.; Fally, F.; Perrichon, V.; Vidal, H.; Hickey, N.; Kašpar, J. Reduction of high surface area CeO_2-ZrO_2 mixed oxides. *J. Phys. Chem. B* **2000**, *104* (39), 9186−9194.

(24) Binet, C.; Daturi, M. Methanol as an IR probe to study the reduction process in ceria-zirconia mixed compounds. *Catal. Today* **2001**, *70* (1−3), 155−167.

(25) Appel, L. G.; Eon, J. G.; Schmal, M. The CO_2−CeO_2 interaction and its role in the CeO_2 reactivity. *Catal. Lett.* **1998**, *56* (4), 199−202.

(26) Zhang, F.; Liu, Z.; Zhang, S.; Akter, N.; Palomino, R. M.; Vovchok, D.; Orozco, I.; Salazar, D.; Rodriguez, J. A.; Llorca, J.; Lee, J.; Kim, D. H.; Xu, W.; Frenkel, A. I.; Li, Y.; Kim, T.; Senanayake, S. D. In situ elucidation of the active state of Co−CeO_x catalysts in the dry reforming of methane: The important role of the reducible oxide support and interactions with cobalt. *ACS catalysis* **2018**, *8* (4), 3550−3560.

(27) Baumann, N.; Lan, J.; Iannuzzi, M. CO_2 adsorption on the pristine and reduced $CeO_2(111)$ surface: Geometries and vibrational spectra by first principles simulations. *J. Chem. Phys.* **2021**, *154* (9), No. 094702.

(28) Kumari, N.; Haider, M. A.; Agarwal, M.; Sinha, N.; Basu, S. Role of reduced $CeO_2(110)$ surface for CO_2 reduction to CO and methanol. *J. Phys. Chem. C* **2016**, *120* (30), 16626−16635.

(29) Slostowski, C.; Marre, S.; Dagault, P.; Babot, O.; Toupance, T.; Aymonier, C. CeO_2 nanopowders as solid sorbents for efficient CO_2 capture/release processes. *Journal of CO_2 Utilization* **2017**, *20*, 52−58.

(30) Zhou, Y.; Liu, D.; Liu, Z.; Feng, L.; Yang, J. Interfacial Pd−O−Ce linkage enhancement boosting formic acid electrooxidation. *ACS Appl. Mater. Interfaces* **2020**, *12* (41), 47065−47075.

(31) Hao, X.; Yoko, A.; Chen, C.; Inoue, K.; Saito, M.; Seong, G.; Takami, S.; Adschiri, T.; Ikuhara, Y. Atomic-Scale Valence State Distribution inside ultrafine CeO_2 nanocubes and its size dependence. *Small* **2018**, *14* (42), No. e1802915.

(32) Hao, X.; Yoko, A.; Inoue, K.; Xu, Y.; Saito, M.; Chen, C.; Seong, G.; Tomai, T.; Takami, S.; Shluger, A. L.; Xu, B.; Adschiri, T.; Ikuhara, Y. Atomistic origin of high-concentration Ce^{3+} in {100}-faceted Cr-doped CeO_2 nanocrystals. *Acta Mater.* **2021**, *203* (15), 116473.

(33) Seong, G.; Dejhosseini, M.; Adschiri, T. A kinetic study of catalytic hydrothermal reactions of acetaldehyde with cubic CeO_2 nanoparticles. *Appl. Catal., A* **2018**, *550*, 284−296.

(34) Yoko, A.; Fukushima, Y.; Shimizu, T.; Kikuchi, Y.; Shimizu, T.; Guzman-Urbina, A.; Ouchi, K.; Hirai, H.; Seong, G.; Tomai, T.;

Adschiri, T. Process assessments for low-temperature methane reforming using oxygen carrier metal oxide nanoparticles. *Chem. Eng. Process. Process Intensif.* **2019**, *142*, No. 107531.

(35) Seong, G.; Yoko, A.; Inoue, R.; Takami, S.; Adschiri, T. Selective chemical recovery from biomass under hydrothermal conditions using metal oxide nanocatalyst. *J. Supercrit. Fluids* **2018**, *133*, 726−737.

(36) Zhang, J.; Kumagai, H.; Yamamura, K.; Ohara, S.; Takami, S.; Morikawa, A.; Shinjoh, H.; Kaneko, K.; Adschiri, T.; Suda, A. Extra-low-temperature oxygen storage capacity of CeO_2 nanocrystals with cubic facets. *Nano Lett.* **2011**, *11* (2), 361−364.

(37) Dejhosseini, M.; Aida, T.; Watanabe, M.; Takami, S.; Hojo, D.; Aoki, N.; Arita, T.; Kishita, A.; Adschiri, T. Catalytic cracking reaction of heavy oil in the presence of cerium oxide nanoparticles in supercritical water. *Energy Fuels* **2013**, *27* (8), 4624−4631.

(38) Zhu, Y.; Seong, G.; Noguchi, T.; Yoko, A.; Tomai, T.; Takami, S.; Adschiri, T. Highly Cr-substituted CeO_2 nanoparticles synthesized using a non-equilibrium supercritical hydrothermal process: High oxygen storage capacity materials designed for a low-temperature bitumen upgrading process. *ACS Applied Energy Materials* **2020**, *3* (5), 4305−4319.

(39) Glogic, E.; Claverie, M.; Jubayed, M.; Musumeci, V.; Carême, C.; Martin, F.; Sonnemann, G.; Aymonier, C. Greening Pathways for Synthetic Talc Production Based on the Supercritical Hydrothermal Flow Process. *ACS Sustainable Chem. Eng.* **2021**, *9* (49), 16597−16605.

(40) Stieberova, B.; Zilka, M.; Ticha, M.; Freiberg, F.; Caramazana-González, P.; McKechnie, J.; Lester, E. Sustainability assessment of continuous-flow hydrothermal synthesis of nanomaterials in the context of other production technologies. *Journal of Cleaner Production* **2019**, *241*, No. 118325.

(41) Kresse, G.; Furthmüller, J. Efficient iterative schemes for ab initio total-energy calculations using a plane-wave basis set. *Phys. Rev. B* **1996**, *54*, 11169.

(42) Kresse, G.; Joubert, D. From ultrasoft pseudopotentials to the projector augmented-wave method. *Phys. Rev. B* **1999**, *59* (3), 1758.

(43) Perdew, J. P.; Burke, K.; Ernzerhof, M. Generalized gradient approximation made simple. *Physical review letters* **1996**, *77* (18), 3865.

(44) Dudarev, S. L.; Botton, G. A.; Savrasov, S. Y.; Humphreys, C. J.; Sutton, A. P. Electron-energy-loss spectra and the structural stability of nickel oxide: An LSDA+ U study. *Phys. Rev. B* **1998**, *57* (3), 1505.

(45) Keating, P. R.; Scanlon, D. O.; Morgan, B. J.; Galea, N. M.; Watson, G. W. Analysis of intrinsic defects in CeO_2 using a Koopmans-like GGA+ U approach. *J. Phys. Chem. C* **2012**, *116* (3), 2443−2452.

(46) Momma, K.; Izumi, F. VESTA 3 for three-dimensional visualization of crystal, volumetric and morphology data. *Journal of applied crystallography* **2011**, *44* (6), 1272−1276.

(47) Izumi, F.; Ikeda, T. In Implementation of the Williamson-Hall and Halder-Wagner methods into RIETAN-FP, Annual Report of the Advanced Ceramics Research Center Nagoya Institute of Technology, 2015; Vol. 3; pp 33−38. http://id.nii.ac.jp/1476/00002383/.

(48) Canchanya-Huaman, Y.; Mayta-Armas, A. F.; Pomalaya-Velasco, J.; Bendezú-Roca, Y.; Guerra, J. A.; Ramos-Guivar, J. A. Strain and grain size determination of CeO_2 and TiO_2 nanoparticles: Comparing integral breadth methods versus rietveld, μ-Raman, and TEM. *Nanomaterials* **2021**, *11* (9), 2311.

(49) Chen, W.; Xue, J.; Bao, Y.; Feng, L. Surface engineering of nano-ceria facet dependent coupling effect on Pt nanocrystals for electro-catalysis of methanol oxidation reaction. *Chemical Engineering Journal* **2020**, *381*, No. 122752.

(50) Chen, L.; Fleming, P.; Morris, V.; Holmes, J. D.; Morris, M. A. Size-related lattice parameter changes and surface defects in ceria nanocrystals. *J. Phys. Chem. C* **2010**, *114* (30), 12909−12919.

(51) Cresi, J. S. P.; Spadaro, M. C.; D'Addato, S.; Valeri, S.; Amidani, L.; Boscherini, F.; Bertoni, G.; Deiana, D.; Luches, P. Contraction, cation oxidation state and size effects in cerium oxide nanoparticles. *Nanotechnology* **2017**, *28* (49), 495702.

(52) Deshpande, S.; Patil, S.; Kuchibhatla, S. V.; Seal, S. Size dependency variation in lattice parameter and valency states in nanocrystalline cerium oxide. *Appl. Phys. Lett.* **2005**, *87*, 133113.

(53) Schilling, C.; Hofmann, A.; Hess, C.; Ganduglia-Pirovano, M. V. Raman spectra of polycrystalline CeO_2: A density functional theory study. *J. Phys. Chem. C* **2017**, *121* (38), 20834−20849.

(54) Wang, L.; Meng, F. Oxygen vacancy and Ce^{3+} ion dependent magnetism of monocrystal CeO_2 nanopoles synthesized by a facile hydrothermal method. *Mater. Res. Bull.* **2013**, *48* (9), 3492−3498.

(55) Varalda, J.; Dartora, C. A.; De Camargo, P. C.; De Oliveira, A. J. A.; Mosca, D. H. Oxygen diffusion and vacancy migration thermally-activated govern high-temperature magnetism in ceria. *Sci. Rep.* **2019**, *9* (1), 4708.

(56) Kang, B.; Vincent, J. L.; Lee, Y.; Ke, L.; Crozier, P. A.; Zhu, Q. Modeling surface spin polarization on ceria-supported Pt nanoparticles. *J. Phys.: Condens. Matter* **2022**, *34* (25), 255002.

(57) Yang, Y.; Wang, S.; Jiang, Y.; Wu, X.; Xia, C.; Peng, R.; Lu, Y. CO_2 activation and reduction on Pt-CeO_2-based catalysts. *J. Phys. Chem. C* **2019**, *123* (28), 17092−17101.

(58) Li, Z.; Werner, K.; Qian, K.; You, R.; Płucienik, A.; Jia, A.; Freund, H. J. Oxidation of reduced ceria by incorporation of hydrogen. *Angew. Chem., Int. Ed.* **2019**, *58* (41), 14686−14693.

(59) Krishna, K.; Bueno-López, A.; Makkee, M.; Moulijn, J. A. Potential rare earth modified CeO_2 catalysts for soot oxidation: I. Characterisation and catalytic activity with O_2. *Applied Catalysis B: Environmental* **2007**, *75* (3−4), 189−200.

(60) Aneggi, E.; Wiater, D.; De Leitenburg, C.; Llorca, J.; Trovarelli, A. Shape-dependent activity of ceria in soot combustion. *ACS Catal.* **2014**, *4* (1), 172−181.

(61) Meunier, F. C.; Tibiletti, D.; Goguet, A.; Reid, D.; Burch, R. On the reactivity of carbonate species on a Pt/CeO_2 catalyst under various reaction atmospheres: Application of the isotopic exchange technique. *Applied Catalysis A: General* **2005**, *289* (1), 104−112.

(62) Ziemba, M.; Schilling, C.; Ganduglia-Pirovano, M. V.; Hess, C. Toward an atomic-level understanding of ceria-based catalysts: when experiment and theory go hand in hand. *Acc. Chem. Res.* **2021**, *54* (13), 2884−2893.

(63) Devi, P.; Verma, R.; Singh, J. P. Advancement in electro-chemical, photocatalytic, and photoelectrochemical CO_2 reduction: Recent progress in the role of oxygen vacancies in catalyst design. *Journal of CO2 Utilization* **2022**, *65*, No. 102211.

(64) Cheng, Q.; Huang, M.; Xiao, L.; Mou, S.; Zhao, X.; Xie, Y.; Jiang, G.; Jiang, X.; Dong, F. Unraveling the influence of oxygen vacancy concentration on electrocatalytic CO_2 reduction to formate over indium oxide catalysts. *ACS Catal.* **2023**, *13* (6), 4021−4029.

(65) Li, M.; Tumuluri, U.; Wu, Z.; Dai, S. Effect of dopants on the adsorption of carbon dioxide on ceria surfaces. *ChemSusChem* **2015**, *8* (21), 3651−3660.